

The impact of local noise recorded at the ET candidate sites on the signal to noise ratio of CBC gravitational wave signals for the ET triangle configuration

Matteo Di Giovanni ^{1,2} Davide Rozza ^{3,4} Rosario De Rosa ^{5,6} Enrico Calloni ^{5,6} Domenico D’Urso ^{7,8,9} Luca Naticchioni ² Annalisa Allocca ^{5,6} Giovanni Luca Cardello ^{7,8,9} Alessandro Cardini ¹⁰ Andrea Contu ¹⁰ Giovanni Diaferia ¹¹ Luciano Errico ^{5,6} Carlo Giunchi ⁹ Jan Harms ^{12,13} Marco Olivieri ¹¹ Piero Rapagnani ^{1,2} Fulvio Ricci ^{1,2} Valeria Sipala ^{7,8} and Lucia Trozzo ⁶

¹*La Sapienza Università di Roma, I-00185 Roma, Italy*

²*INFN, Sezione di Roma, I-00185 Roma, Italy*

³*INFN, sezione di Milano Bicocca, I-20126, Milano, Italy*

⁴*Università di Milano Bicocca, I-20126, Milano, Italy*

⁵*Università Federico II Napoli, I-80126 Napoli, Italy*

⁶*INFN - sezione di Napoli, I-80126 Napoli, Italy*

⁷*Department of Chemistry, Physics, Mathematics and Natural Science, Università degli Studi di Sassari, I-07100, Sassari, Italy*

⁸*INFN, sezione di Cagliari, I-09042, Monserrato (Cagliari), Italy*

⁹*INGV, Sezione di Pisa, I-56125, Pisa, Italy*

¹⁰*INFN - sezione di Cagliari, I-09042, Monserrato (Cagliari), Italy*

¹¹*INGV, Sezione di Bologna, I-40127, Bologna, Italy*

¹²*Gran Sasso Science Institute, I-67100, L’Aquila, Italy*

¹³*INFN, Laboratori Nazionali del Gran Sasso, I-67100, Assergi (L’Aquila), Italy*

(Dated: March 5, 2025)

We present an evaluation of how site dependent noise can affect the signal to noise ratio (SNR) of compact binary coalescence (CBC) signals in the future 3rd generation gravitational wave (GW) detector Einstein Telescope (ET). The design of ET is currently pushing the scientific community to study its scientific potential with respect to known, and possibly unexpected, GW signals using its design sensitivity curves. However, local ambient noise may have an impact on the ET sensitivity at low frequency and therefore affect the SNR of CBC signals at low frequency. Therefore, we study the impact of ambient noise on the ET sensitivity curve at the two sites candidate to host ET - Sardinia, in Italy, and the Euregio Meuse-Rhine (EMR) at the Netherlands-Belgium border - and infer the impact on the ET sensitivity curve and how the SNR of CBC signals at low frequencies is affected. We find that Sardinia shows results which are on par, if not better, than the design case. On the other hand, ambient noise for the current EMR sensitivity curve in Terziet causes a higher degradation of the SNR performances.

I. INTRODUCTION

With the successful exploitation [1–3] of current 2nd generation gravitational wave (GW) detectors, namely Advanced Virgo (AdVirgo), located in Italy [4], Advanced LIGO Hanford and Livingston (aLIGO), located in the United States [5] and KAGRA in Japan [6], the scientific community started to thoroughly investigate [7, 8] the prospects of future 3rd generation GW detectors that are expected to start observations in the mid 2030s, i.e., Cosmic Explorer (CE) [9–11] and the Einstein Telescope (ET) [12–15], with the latter being the subject of this work. ET was first proposed in 2010 and the foreseen improvements with respect to current-generation detectors include the extension of the observation bandwidth from the current limit of about 20 Hz to 2 Hz and an improvement of the sensitivity up to a factor 8 across the band covered by current detectors [15].

For what concerns the configuration of ET, there are two proposals under consideration. The most recent one is that of a detector network composed by two widely separated L-shaped detectors with 15 km long arms [8, 16]. On the other hand, the original project foresees three

pairs of nested interferometers arranged in an equilateral triangle (also called xylophone configuration, Figure 1) with the sides 10 km long [12–15]. For each interferometer pair, one detector is optimized for low frequencies ($2 \text{ Hz} < f < 40 \text{ Hz}$) and the other for high frequencies ($f > 40 \text{ Hz}$). Since recently, moving the lower limit to 3 Hz is being considered as well [15], but, to be on the conservative side, we keep using the 2 Hz lower limit for this work. In both the 2L and the triangle configurations, ET will be hosted underground, at a currently planned depth between 200 m and 300 m to reduce seismic motion at the input of the suspension system of the mirrors and to reduce the impact of atmospheric disturbances [17] and Newtonian noise (NN). In this work, since it poses the most challenges from the point of view of environmental noise mitigation, we focus on the ET triangular configuration.

Generally speaking, the extension of the bandwidth to 2 Hz and the sharp increase in sensitivity will significantly improve the rate of detected events giving the possibility to issue early warnings for the coalescence of compact objects (CBC) several minutes, if not hours depending on the source, before the merger [7, 8, 18–20]. In fact, with

respect to current detectors, CBC signals will spend more time in the ET accessible bandwidth, therefore enabling early detection and sky localization. As it was demonstrated by GW170817 [21–24], this is extremely important in the case of binary neutron star (BNS) mergers. As a matter of fact, joint multimessenger observations with electromagnetic observatories are paramount to exploit the scientific potential of BNS events and shed new light on the internal structure of neutron stars [7]. In particular, depending on the distance of the source and requiring a signal-to-noise ratio (SNR) ≥ 12 and a sky localization smaller than 100 deg^2 , ET is expected to be able to send early warnings between 1 and 20 hours before the BNS merger [7]. The release of an early warning increases the chances of detection for the electromagnetic counterparts. Astronomers would be able to point the telescope in the region of the signal to start the monitoring to obtain pre-merger images as well as merger. This enables to detect the early electromagnetic emission, which is fundamental to understand the physics of the emission mechanism and the merger remnant [7].

The significant increase in sensitivity below 100 Hz will also allow for more detailed observations about the merger of intermediate mass black holes (IMBH) [7, 25–27], i.e. black holes (BH) with masses in the $[10^2, 10^5] M_\odot$ range. Their typical merger frequency is $< 100 \text{ Hz}$ and the signals are expected to spend a maximum of $\mathcal{O}(100 \text{ s})$ in the ET bandwidth. Currently, GW detectors are limited to BH masses $\mathcal{O}(100 M_\odot)$ and hypothetical IMBH merger signals are typically only detectable in very short time intervals of a few milliseconds. On the other hand, ET will open the possibility of detecting these IMBH, studying the possibility that they are the seeds of the supermassive BHs in the center of galaxies [7, 27]. Furthermore, a precise reconstruction of waveforms for compact objects during inspiral and merger will allow accurate tests of General Relativity.

Therefore, any degradation with respect to design in the low-frequency sensitivity of ET may significantly hinder the capability of early detections and multimessenger observations for BNS mergers and may reduce the quality of the observations for IMBH [8, 19]. As a consequence, since seismic disturbances, of both natural [28–40] and anthropogenic [32, 34, 39, 41–43] origin, are the main source of noise limiting the detector sensitivity at low frequency and can affect GW data in many ways [34, 39, 44–53], seismic characterization studies at the candidate sites to host ET are paramount. The goal is to guarantee a suitable environment for this future detector that makes the reaching of its design sensitivity possible [54] through appropriate design of noise suppression systems.

As of 2024, there are two sites which are officially candidate to host the ET triangle (Figure 2): the Euregio Meuse-Rhine (EMR) [14, 15], between Belgium and the Netherlands, and the area surrounding the Sos Enattos former mine in Sardinia (Italy) [14, 15, 55–58].

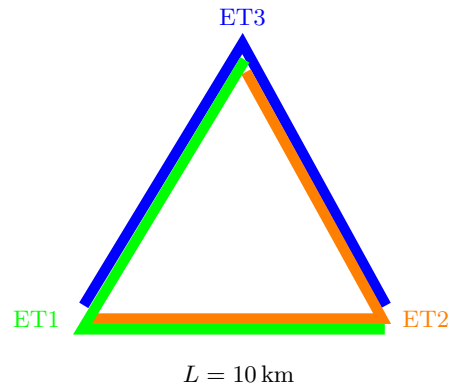


FIG. 1: *Scheme of the ET xylophone for the triangular configuration. Each detector ET1,2,3 is composed of an interferometer optimized for low-frequency detection and another optimized for high-frequency detection for a total of six.*

Since 2014, the Sos Enattos [55–60] and EMR [61–63] sites have been the subject of characterization studies aimed at assessing their suitability to host ET. However, except [59] and the recent work published by [64], no works are assessing the impact of site dependent noise on the detectability of GW sources. Therefore, the scope of this paper is to provide a first estimation of how site dependent low-frequency noise may affect the SNR of CBC signals after modifying the ET sensitivity curve according to the actual seismic noise measured at each of the aforementioned ET candidate sites. We think that this approach may provide some relevant information for both the site selection process and the design of noise suppression systems for ET. In particular, extending the methodology already shown in [59] and [65], we investigate the case of IMBH and BNS focusing on the $[2, 10] \text{ Hz}$ range, where ambient noise is more prominent [57–59] and may affect early warnings. Beyond 10 Hz, noise contributions from the detector hardware dominate the noise budget and, therefore, are out of the scope of our work. As a consequence of the focus in the low frequency range, our goal is not to claim whether a merger will be detected or not (merger frequencies are way beyond the considered frequency range), but only if it will be possible to observe the inspiral preceding the merger for multimessenger purposes. On the other hand, the details of how parameter estimation and other cosmological implications would be affected are beyond the goal of this work and will not be discussed here, but may represent one of the future developments of this study.

The paper is organized in the following way: in Section II we discuss the astrophysical background of this study; the method is presented in Section III; Section IV talks through the data used for this study; the results are discussed in Section V and VI, whereas Section VII gives a qualitative contribution to the discussion regarding the triangle and 2L configurations. Finally, the conclusions are debated in Section VIII.



FIG. 2: Map of Europe showing the locations of the candidate sites considered in this work. The village of Terziet in the Netherlands is usually taken as a reference for the EMR candidate site. The maps are taken from [66–68] and modified according to the creative commons license 3.0. The orientation of the triangle icons is not representative of the actual proposed orientations for the ET detector for each site.

II. ASTROPHYSICAL BACKGROUND

For a long time, scientists questioned about the existence of a class of black holes, identified as IMBH [25–27], between those formed by stellar collapse (i.e. $M < 10^2 M_\odot$) and the supermassive BH at the centers of galaxies (i.e. $M > 10^5 M_\odot$). Before the third observing run (O3) [69] of aLIGO and AdVirgo, there was no clear evidence about their existence and the gap between $[10^2, 10^5] M_\odot$ remained unexplained. During the third observing run (O3) of the LIGO-Virgo detectors, GW190521 [70], consistent with two BH merging to form a $\simeq 140 M_\odot$ remnant, provided the first direct evidence of IMBH formation. During the same observing run, a few more marginal candidates for IMBH formation were found, but none sufficiently significant to indicate detection of further IMBH mergers [69, 71].

The formation channel of IMBH has not been completely established. A possible explanation is that they may have formed via the subsequent, usually referred to as hierarchical, mergers of lighter BH [72]. Other IMBH formation channels also include the direct collapse of massive first-generation, low-metallicity Population III stars [27]. The existence of IMBH and their accretion through hierarchical mergers may also provide relevant information about the formation of supermassive BH [69].

Since the merger frequency of two compact objects orbiting around each other is inversely proportional to their chirp mass $M_c \equiv \frac{(m_1 m_2)^{3/5}}{(m_1 + m_2)^{1/5}}$ as $f_{GW} \propto M_c^{-5/8}$, a BH binary with component masses in the IMBH range merge at relatively low frequencies, i.e. $f < 100$ Hz. For example, using the Keplerian approximation for circular orbits and considering the two BH as merged when their orbital

separation is less than the Schwarzschild radius

$$R_s = \frac{2Gm}{c^3}, \quad (1)$$

an equal mass IMBH with $m_1 = m_2 = 100 M_\odot$, each with $R_s \simeq 533$ km, has an orbital frequency at merger [73]

$$\omega_k(R_s) = \sqrt{\frac{Gm_{\text{tot}}}{R_s^3}} \simeq 420 \text{ Hz}, \quad (2)$$

which gives an approximate merger frequency of

$$f_{GW} = \frac{\omega_{GW}}{2\pi} = \frac{\omega_k}{\pi} \simeq 133 \text{ Hz}. \quad (3)$$

Furthermore, if we calculate the number of cycles spent in a given frequency band $[f_{\text{min}}, f_{\text{max}}]$ [73]

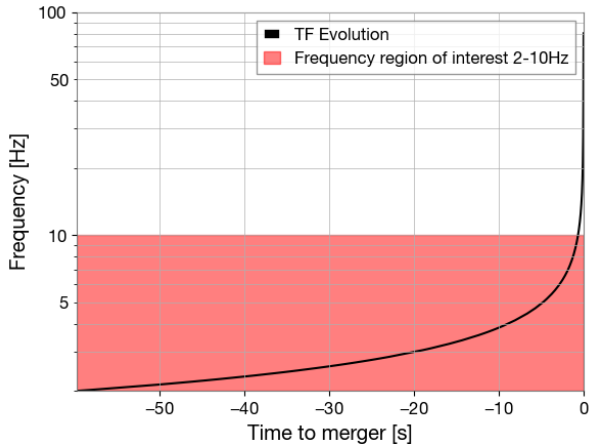
$$\mathcal{N}_{\text{cyc}} = \frac{1}{32\pi^{8/3}} \left(\frac{GM_c}{c^3} \right)^{-5/3} (f_{\text{min}}^{-5/3} - f_{\text{max}}^{-5/3}), \quad (4)$$

we find that most of the cycles of the observable waveform are contained in $[2, 10]$ Hz. At cosmological distances within the reach of ET [7], redshift z also contributes to lowering the observed merger frequency as masses observed on Earth in the detector frame have to be corrected as $m_{\text{det}} = m_{\text{sour}}(1+z)$.

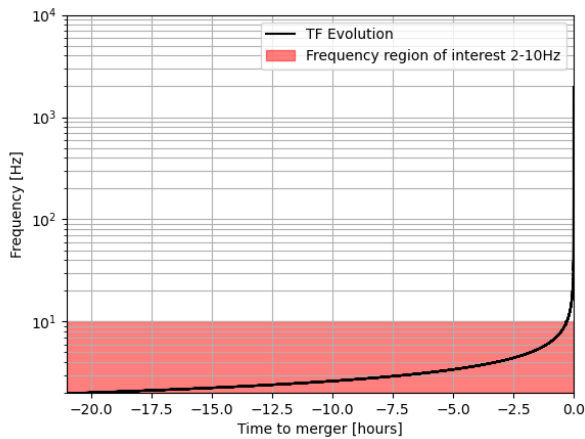
Figure 3a shows the time-frequency evolution of an equal mass $m_{\text{tot}} = 200 M_\odot$ IMBH in the circular orbit, non spinning case computed using the IMRPhenomD waveform approximant [74, 75]. In this case, the merger frequency appears to be $f_{\text{merge}} \simeq 82$ Hz, lower than what is shown in Equation 3. This is due to the fact that GW waveform approximants take into account relativistic effects close to the merger. In fact, we refer to the innermost stable circular orbit (ISCO) as the last orbit beyond which stable circular orbits are no longer allowed. For the case mentioned above, $f_{\text{ISCO}} \simeq 11$ Hz. In particular, IMRPhenomD is based on a combination of analytic post-Newtonian (PN) and effective-one-body (EOB) methods to describe the inspiral, whereas the merger phase is calibrated using numerical relativity models [74, 75]. Figure 3a also highlights the importance of the $[2, 10]$ Hz band, in which an IMBH spends most of the time before the merger.

BNS, on the other hand, are a completely different source. They are composed of two NS, have an expected total mass between $2.2 M_\odot$ and $4.4 M_\odot$ and merge at frequency $\mathcal{O}(\text{kHz})$. All the relevant information carried by GW about the physics of neutron stars can be found in the high-frequency part of the signal as well. However, low-frequency detection plays a crucial role in the observation of BNS mergers. In fact, as mentioned in Section I, detecting a BNS as soon as possible may not only significantly increase the observation rate [8, 19, 77], but also allow for precise sky localization [20] and sending prompt early warnings to observatories for conducting multimessengers observing campaigns

III. METHODOLOGY



(a) Time-frequency evolution of an equal mass IMBH with $m_{\text{tot}} = 200 M_{\odot}$ in the circular orbit, non spinning case simulated using the IMRPhenomD waveform approximant [74, 75].



(b) Time-frequency evolution of an equal mass BNS with $m_{\text{tot}} = 2.8 M_{\odot}$ in the circular orbit, non spinning case simulated using the IMRPhenomPv2_NRTidalv2 waveform approximant [76].

FIG. 3: Examples of time-frequency evolution of CBC signals.

[7, 18]. Moreover, BNS typically spend several hours at low frequency accumulating SNR before the chirp. Figure 3b shows the time-frequency evolution of an equal mass $m_{\text{tot}} = 2.8 M_{\odot}$ BNS underlining the fact that it spends $\simeq 20$ hours in the $[2, 10]$ Hz band. Furthermore, Equation 4 shows that $\mathcal{N}_{\text{cyc}}([2, 10] \text{ Hz}) \simeq 7 \times 10^5$ and $\mathcal{N}_{\text{cyc}}([2, 4096] \text{ Hz}) \simeq 7.6 \times 10^5$. This means that only fully accomplishing the low-frequency design sensitivity, especially below 10 Hz, may allow to exploit the potential of ET for what concerns multimessenger astronomy [8, 19].

To estimate the impact of site-dependent noise over the SNR of CBC events, we first calculate how site noise changes the ET design sensitivity curve. For this study we use the design curve already applied for [8]. Depending on the frequency band, different contributions affect the ET noise budget curve like seismic, Newtonian, thermal, and quantum noise. Among these noise sources, the dominant contribution in the frequency region between 2 and 10 Hz is the NN. Beyond 10 Hz, other contributions, like quantum and thermal noise from the detector hardware, dominate the noise budget [53, 78–80]. NN is caused by gravity fluctuations from mass distributions that change around the detector with time. These fluctuations are generated by variations of atmospheric and ground densities in the vicinity of the test masses of the detectors. Ground density variations are caused by ground motion, i.e., seismic waves, which are the only contribution to NN considered in this work. Atmospheric NN is not taken into account due to the current lack of dedicated environmental sensors installed at the ET candidate sites.

We estimate the NN contribution of the ET sensitivity between 2 Hz and 10 Hz as [80]

$$\tilde{h}_{\text{NN}}(f) = \frac{4\pi}{3} G \rho_0 \frac{2\sqrt{2}}{L} \frac{1}{(2\pi f)^2} \tilde{x}(f), \quad (5)$$

where the frequency (f) dependence of the NN budget (\tilde{h}_{NN}) is related to the gravitational constant (G), the density of the ground medium (ρ_0), the size of the arm-length of each interferometer (L) and the amplitude spectral density (ASD) of the seismic displacement (\tilde{x}). Equation 5 can be derived from

$$\delta \vec{a}(\omega) = \frac{4\pi}{3} G \rho_0 \left(2\vec{\xi}_P(\omega) - \vec{\xi}_S(\omega) \right), \quad (6)$$

which is Equation 5 of [59] and Equation 6 of [80], where $\vec{\xi}_{P,S}$ is the seismic displacement vector for the compressional (P) and shear (S) waves, respectively, and ω is the angular frequency. Equation 5 holds for a spherical cavern in an infinite homogeneous medium as it is clearly stated after Equation 6 of [80]. An even more detailed derivation can be found in Section 3.3 of [53]. In general, equation 5 is evaluated assuming:

- underground seismic spectra representative of body waves only;
- one third of the body waves contribution is from compressional waves;
- surface waves are negligible at depths of a few hundred meters;
- uncorrelated NN on the interferometer test masses.

In addition to that, Equation 5 does not include any suppression factor from NN mitigation systems.

Referring to equation 5, the used ASD \tilde{x} are the percentiles (10th, 50th, and 90th) of the spectral distributions calculated on 120s windows for the vertical and horizontal channels of the seismometers. The length of the time window is chosen according to the typical maximum duration of an IMBH signal (Figure 5b) and on the time segment duration proposed for CBC multiband analysis for BNS [20]. Under these assumptions, the ET noise budget that we use takes into account the NN evaluated from the seismic noise of each candidate site for the 10th, 50th, and 90th percentile of seismic spectra. Since a simple projection alone does not show the effect of non-stationarity of NN (from now on defined glitchness) we also use a more effective indicator, called the Noise to Target Ratio (NTR) and derived from [59] as:

$$NTR = \sqrt{\frac{1}{\Delta f} \int_{f_1}^{f_2} df \frac{S_n(f)}{S_{n,ET}(f)}}, \quad (7)$$

where the $S_{n,ET}(f)$ is the PSD of the ET design sensitivity, whereas $S_n(f)$ is the PSD of the modified ET sensitivity, where the NN is substituted with the contribution of the local noise over the chosen time window and $\Delta f = f_2 - f_1$ is the selected bandwidth. This way, the NTR is evaluated time by time and normalised for the comparison of the two candidate sites.

After inferring the modified ET sensitivity curves, we gather the events of interest for our study from astrophysical catalogs and we use PyCBC [81] to generate and inject signals in simulated ET noise. Waveforms are generated using the IMRPhenomD [74, 75] GW approximant for IMBH and IMRPhenomPv2_NRTidalv2 [76] for BNS, both available in the LIGO-Virgo-KAGRA Algorithm Library (LAL) [82]. To take into account the antenna pattern of the detector, the ET triangle is simulated considering three properly oriented L-shaped co-located detectors, with an arm length of 10 km and an arm angle of 60°. The variation of the antenna pattern with time is also taken into account. Since the actual orientation of the ET triangle has not been decided yet, we choose an arbitrary positioning of the detector. For the Sardinia candidate site, ET is assumed to be located at the Sos Enattos mine at [40.44° N, 9.44° E], whereas for the EMR site, we have chosen the village of Terziet at [50.73° N, 5.91° E] as a reference. For each detector, noise is obtained by generating white noise colored according to the given sensitivity curve and the same sources are taken into account. Waveforms are injected into the noise of each detector composing ET (labeled ET1, ET2 and ET3 respectively).

First, we infer the distribution of the SNR of the signals injected in simulated noise obtained using the ET design sensitivity. Signal SNR is calculated as

$$SNR = \sqrt{MSNR_{ET1}^2 + MSNR_{ET2}^2 + MSNR_{ET3}^2}, \quad (8)$$

where $MSNR_{ET1,2,3}$ are the matched filter SNR calculated in each detector. Then, using the same events, we

repeat the procedure for each curve inferred from Equation 5 using the 10th, 50th and 90th percentile seismic spectra. The new SNR distributions are then compared against the design case used as a benchmark. The distributions of the SNR losses are obtained after calculating, for each event, the ratio between the new SNR and the benchmark SNR.

To calculate the MSNR, we assume the signal to exhibit the two polarization states[83]

$$h_+(t) = -A(t) \frac{1 + \cos^2(\iota)}{2} \cos[2\phi_c + 2\phi(t)], \quad (9)$$

$$h_\times(t) = -A(t) \cos^2(\iota) \sin[2\phi_c + 2\phi(t)], \quad (10)$$

where $A(t)$ is the amplitude, ι the inclination of the source, ϕ_c the phase of the signal at the chirp and $\phi(t)$ the phase of the signal. Therefore, MSNR is calculated as [84]:

$$MSNR^2(t) = \frac{(s|h_{cos})^2 + (s|h_{sin})^2}{(h_{cos}|h_{cos})} \quad (11)$$

with

$$(s|h)(t) = 4\text{Re} \int_{f_{\min}}^{f_{\max}} \frac{\tilde{s}(f)\tilde{h}^*(f)}{S_n(f)} e^{2\pi i f t} df \quad (12)$$

where $\tilde{s}(f)$ is the Fourier Transform (FT) of the data, $\tilde{h}^*(f)$ is the FT of the template and h_{cos}/h_{sin} are the two orthogonal phase components of the template shown in Equations 9 and 10 [83, 84]. In our case, $f_{\min} = 2$ Hz and $f_{\max} = 10$ Hz because, as mentioned above, we consider ambient noise only which modifies the ET sensitivity curve not beyond the [2, 10] Hz range. Moreover, taking into account Equations 11 and 12 we note that MSNR out of this bandwidth gives the same contribution to the total MSNR in all cases and would not bring relevant information. Therefore we restrict the calculation between 2 Hz and 10 Hz only. We also point out that we assume perfect knowledge of the source, i.e., matched filter is calculated using the same waveform template injected in the data.

IV. DATA

A. Seismic

Seismic data from the candidate sites come from a set of instruments installed to assess the quality of the sites and for site characterization studies. In particular, data from the Sardinia site come from two seismometers installed in boreholes at ~ -264 m and ~ -252 m at the two proposed vertex locations for the ET triangle known as P2 and P3. The seismometers are Trillium 120 SPH2 coupled with a Nanometrics Centaur CTR4-6S, 6-ch 24-bit data logger. For what concerns the EMR site,

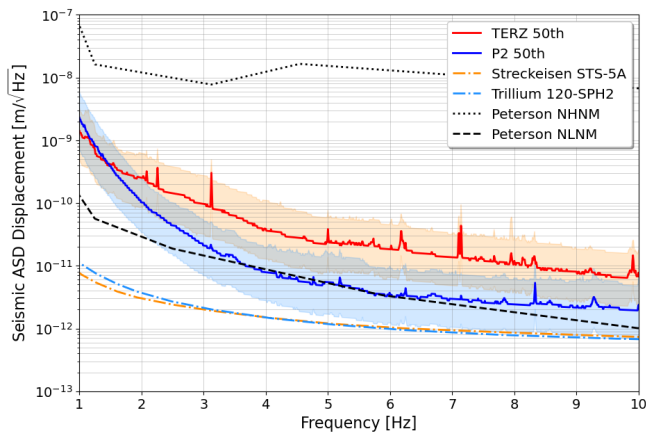


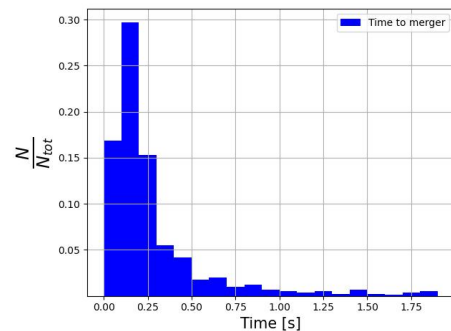
FIG. 4: Seismic ASD displacement for the two candidate sites, TERZ in red and P2 in blue, are reported as a percentile (50th in solid line while 10th and 90th the lower and upper limit of the colored band). Peterson limits (NLNM in black dashed line and NHNM in black dotted line) and the self-noise of both sensors (dash-dot line) are also shown.

the only available data are from a Streckeisen STS-5A borehole seismometer in Terziet, referred to as TERZ, at ~ -250 m. For this reason, we use TERZ as a reference for the EMR candidate site. In both cases, the time period used for the analysis covers two years, from December 21st, 2021 to December 20th, 2023. This period of 730 days has a duty cycle $> 90\%$ at both sites. As mentioned above, the ASD time window is 120 s and the percentiles (10th, 50th, and 90th) for each station are evaluated for all three orthogonal channels (the two horizontal components and the vertical one). Data from P3 shows a lower noise level with respect to P2 in all the channels by an average factor of around 20% between 1 and 10 Hz. For this reason, we will compare P2 and TERZ.

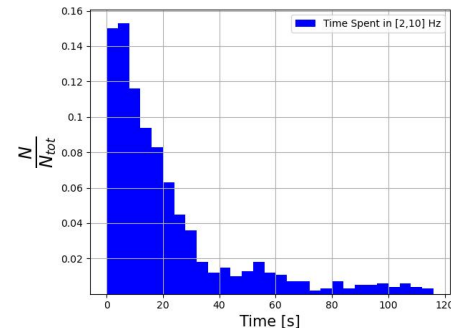
Figure 4 shows the comparison of the percentiles of the vertical component for P2 (in blue) and TERZ (in red) with respect to the Peterson New Low and High Noise Model (NLNM in black dashed line and NHNM in black dotted line respectively) [85]. Above 6 Hz, the P2 data lie on the self-noise of the sensor, making apparent the quietness of the site. We will use these data in Section V as input parameters for the determination of the ET sensitivity curve.

B. Astrophysical Sources

The parameters for IMBH and BNS mergers are taken from the catalog [86] used to produce the results of [8], which considers a set of sources spanning one year between the mock dates 01-01-2030 and 12-31-2030. For what concerns BBH, the catalog results from the mixture of BBH from isolated binary evolution, dynamical forma-



(a) Distribution of the time to merger at 10 Hz for the BBH events considered in this work.



(b) Distribution of the time spent in the $[2, 10]$ Hz range for the BBH events considered in this work.

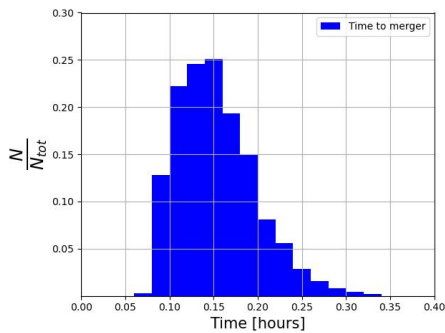
FIG. 5: Times distributions for the IMBH of this work.

tion in young, globular and nuclear star clusters. Masses, spins, redshifts and luminosity distances have been obtained with the open-source code FASTCLUSTER [87]. For this work, we select the events that satisfy the following conditions:

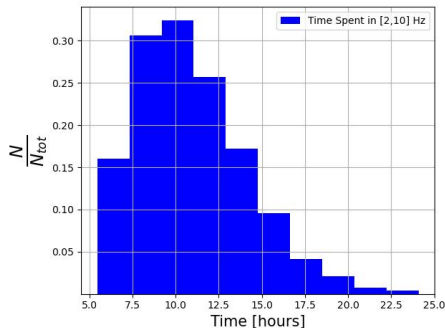
- BBH with at least one source frame component mass above $100 M_{\odot}$;
- BBH with both source frame component mass above $100 M_{\odot}$;
- BBH with a total mass above $100 M_{\odot}$.

for a total of $\simeq 10^3$ events. Figure 5a shows the distribution of the time to the merger at 10 Hz for these events. We note that once left the frequency band considered in this work, most events have less than 0.5 s before merging. On the other hand Figure 5b shows the time spent in the $[2, 10]$ Hz range and points out how most of the time IMBH lie in this bandwidth before the merger.

For BNS mergers, the source frame masses of the two objects are sampled uniformly in the interval $[1.1; 2.5]M_{\odot}$ so that $m_1 > m_2$. Redshifts and luminosity distances are taken from [88]. Since [86] contains $\mathcal{O}(7 \times 10^5)$ BNS events, to limit the computational cost



(a) Distribution of the time to merger at 10 Hz for the BNS events considered in this work.



(b) Distribution of the time spent in the [2, 10] Hz range for the BNS events considered in this work.

FIG. 6: Times distributions for the BNS of this work.

and time of the analysis we randomly sample, using a logarithmic distribution in redshift to privilege closer - therefore stronger - signals, 10^3 events at $z < 1.5$. As mentioned, the BNS signal should reach $SNR \geq 12$ to issue an early warning between 20 hours and 1 hour before the merger. Figure 6a shows the distribution of the time to the merger at 10 Hz for the selected BNS events. We note that, once left the [2, 10] Hz frequency band, most events have less than 20 min before merger. Figure 6b shows the time spent in the [2, 10] Hz range. The relevance of this bandwidth is apparent, since several hours are spent here.

For both IMBH and BNS, the sky position and coalescence phase are sampled uniformly in the entire sky and between $[0, 2\pi]$, respectively. The inclination angle is sampled from a uniform distribution between $[-\pi, \pi]$ and the polarization angle is sampled uniformly in the interval $[0, \pi]$. For simplicity, we are also assuming the circular orbit case. Moreover, to take redshift into account, source frame masses are converted into the detector frame as $m_{det} = m_{sour}(1 + z)$.

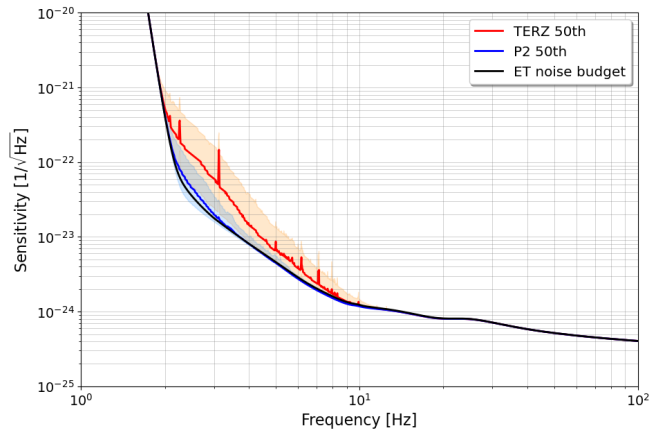


FIG. 7: Sensitivity curves for the two candidate sites, reporting the percentile (50th in solid line while 10th and 90th the lower and upper limit of the colored band) for TERZ (in red) and P2 (in blue), compared with the ET design sensitivity (black).

V. MODIFIED ET CURVES

The ET sensitivity, modified according to what described in Section III, takes into account the local seismic component of the NN of the two candidate sites. In equation 5, we assume $\rho_0 = 2.7 \cdot 10^3$ kg/m³ and $L = 10$ km. Figure 7 reports the sensitivity curve using the NN from P2 and TERZ compared with the ET design noise budget as reported in [8] for the frequency range between 1 Hz and 100 Hz.

To quantify the modified ET sensitivity with respect to the designed one, we evaluated the NTR index defined in Sec. III. While Fig. 7 shows the level of the NN inside the ET sensitivity averaged over two years, the NTR, computed every 120 s, gives information on how many times the modified sensitivity ($S_n(f)$) is above (> 1) or below (< 1) the designed one ($S_{n,ET}(f)$), i.e., information related to the glitchiness of the site. Focusing our attention on the frequency range between $f_1 = 2$ Hz and $f_2 = 10$ Hz, a value of NTR larger than one implies that, in the selected dataset, the contribution of the NN is limiting the ET sensitivity. The higher the NTR, the higher the probability of losing the GW signals. One has to remember that if the bandwidth of the GW signal is larger than f_2 it is possible to recover the signal since the NN is not significant at higher frequencies.

Figure 8 reports the NTR normalised probability distribution for P2 and TERZ. It is possible to note that P2 is characterised by a lower noise and the majority of the data are distributed around $NTR = 1$. To emphasize the difference, we evaluated the cumulative density function (CDF) of the two distributions. The x-axis of Fig. 9 is the NTR and the y-axis represents the CDF confined between 0 (no data are below the specific NTR) and 1 (all data are below that specific NTR). We reported in Table I the value of the NTR corresponding to the specific per-

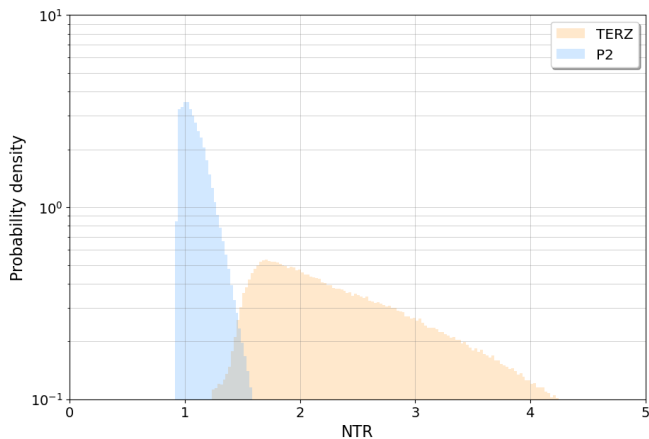


FIG. 8: *NTR* normalised probability distribution for the two sites: P2 (in blue) and TERZ (in red).

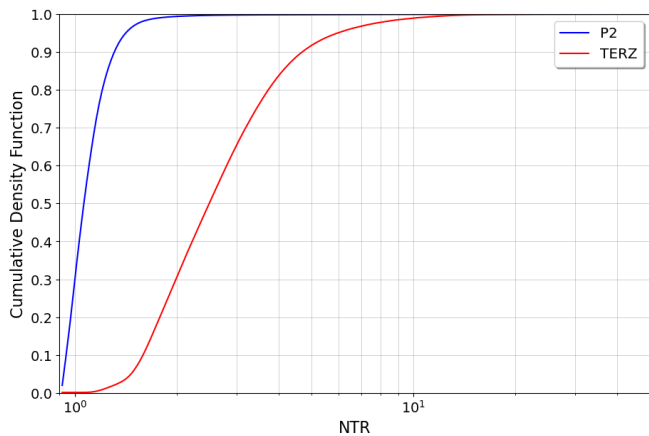


FIG. 9: *Normalised cumulative density function of the NTR normalised distribution, of Fig. 8, for the two sites: P2 (in blue) and TERZ (in red).*

centile for the two sites and in different time periods. The first set of data regards the whole period of two years, 90% of the P2 data are below $NTR = 1.31$, while the same amount of data for TERZ are below $NTR = 4.69$. We performed the analysis separating working days and weekends, day and night hours. The noise is less on both weekends and nights giving information on the anthropogenic origin of this noise related to human activities. Moreover, this human noise is affecting more the TERZ site, while for P2 the variation is less significant.

VI. IMPACT ON SIGNAL TO NOISE RATIO

A. Intermediate Mass Black Holes

Figures 10 and 11 show the SNR distributions for the IMBH case for the Sardinia and EMR candidate sites, respectively. The benchmark SNR distribution inferred us-

ing the design ET sensitivity curve is shown in green. The results are also summarized in Table II. In both cases, we analyze the same 970 events. For the analysis and visualization, we also exclude all those events which have $SNR < 12$ in the best noise condition already. These events never reach the $SNR = 12$ threshold at 10 Hz also when the noise worsens and therefore are not relevant for the scope of this work. On the contrary, this cut guarantees that events eventually lost in the design case, but recovered in the best noise conditions, are retained. This can also highlight any possible improvement of the performances with respect to the expectations.

In Sardinia, on average, the 10th and 50th percentile cases show comparable results (Figures 10a and 10b). The SNR shows a gain of $\simeq 6\%$ and $\simeq 5\%$, respectively (Figures 10d and 10e). The non overlapped green histogram bin, on the left of the $SNR = 12$ threshold, highlights a marginal improvement ($\simeq 2\%$) in the fraction of recovered events for the 10th and 50th percentiles with respect to the design case. On the other hand, in the 90th percentile case the performance is on par with the design case: there is a marginal SNR loss ($\simeq 2.5\%$ - Figure 10f) and the fraction of lost events is consistent with the forecast of the design performance (Figure 10c).

For the EMR site, the situation is different. The 10th percentile case is on par with the design performance, with the SNR showing a gain of $\simeq 2.5\%$ (Figures 11a and 11d). In the 50th percentile, the SNR distribution starts to deviate from the design case, with 5% of events below threshold and a SNR loss $\simeq 12\%$ (Figures 11b and 11e). The 90th percentile shows, as expected, the worst performance with an average SNR loss $\simeq 37\%$ and 24% of events with $SNR \leq 12$ in the considered bandwidth (Figures 11c and 11f). Table II also shows the mean of the ratio between the SNR of the events in Sardinia and the SNR of the events at EMR.

B. Binary Neutron Stars

Figures 12 and 13 and Table III show the results obtained in the case of BNS signals. As for the previous results, we exclude events with $SNR < 12$ in the best noise case. In general, the results are consistent with the IMBH case. In the 10th percentile case, we appreciate a 2% improvement in the fraction of recovered events with respect to the design case. For the 10th, 50th and 90th percentile cases, we find $\simeq 0.05\%$ and $\simeq 3\%$ of events below threshold in the $[2, 10]$ Hz range, respectively. These figures are on par, if not slightly better, with respect to the design case (Table III). In all cases, the ratios between the reconstructed SNR and the design SNR show only marginal differences (Figures 12d, 12e and 12f).

On the other hand, the EMR site shows less promising performances. The 10th percentile case (Figures 13a and 13d) equals the figure of the benchmark case, with a SNR gain $\simeq 2\%$ and 1% more events recovered than the design case. The 50th and 90th percentile show the worst

Percentile	Whole Period		Working days		Weekends		Days		Nights	
	P2	TERZ	P2	TERZ	P2	TERZ	P2	TERZ	P2	TERZ
10th	0.94	1.59	0.94	1.66	0.94	1.49	0.96	1.84	0.93	1.44
50th	1.06	2.49	1.08	2.68	1.04	2.11	1.09	2.84	1.01	1.86
90th	1.31	4.69	1.33	4.96	1.25	3.81	1.34	4.94	1.20	3.68

TABLE I: *NTR values at the specified percentile (10th, 50th, and 90th) for both sites and in different conditions (whole period of two years, working day, weekends, days, nights).*

Case	SNR/SNR _{DESIGN}		EVENTS WITH SNR < 12		SNR _{EMR} /SNR _{SAR}
	Sardinia	EMR	Sardinia	EMR	
10th percentile	+6%	+2.5%	-2%	-1%	0.96
50th percentile	+5%	-12%	-2%	4%	0.83
90th percentile	-2.5%	-37%	2%	24%	0.69

TABLE II: *Summary of the SNR performance for the Sardinia and EMR candidate sites in the case of IMBH signals. The negative figures under the events with SNR < 12 highlight an improvement in the fraction of recovered events with respect to the design case.*

performance and loose $\simeq 6.5\%$ and $\simeq 22\%$ of events, respectively (Figures 13b and 13c). For what concerns the SNR ratios (Figures 13e and 13f), the figures are consistent with the IMBH case and both sites show a loss which is in line with what has been already discussed in Section VI A. Table III also shows the mean of the ratio between the SNR of the events in Sardinia and the SNR of the events at EMR.

Since the time to merger at detection is a relevant information for multimessenger studies, we also provide the cumulative distributions of the fraction of detected events vs. the time to merger at the moment in which the threshold SNR = 12 is reached. (Figures 14 and 15). At the EMR site, we notice that in the worst possible scenario only 11% of events are detectable within 12 minutes from merger, whereas, in the best noise conditions, this fraction improves to 45%. For the 50th percentile case, on the other hand, the fraction is 30%. In Sardinia the difference between the three cases is less apparent, since the fraction of events detectable within 12 minutes from merger oscillates between 40% and 47%.

VII. SNR IN THE TRIANGLE VS. 2L CASE DISCUSSION

All the results shown so far are valid for the ET triangle configuration. Nevertheless, they can already be used to make some qualitative comments for the ongoing discussion regarding the choice of the definitive configuration of ET, i.e., whether it would be a triangular or 2L detector. In fact, in the triangle configuration, the total SNR is given by the sum in quadrature of the single detector SNR:

$$SNR_{3net} = \sqrt{SNR_1^2 + SNR_2^2 + SNR_3^2}. \quad (13)$$

In the ideal case, we assume that each detector in the network observes an event with approximately the same

$SNR \simeq SNR_1 \simeq SNR_2 \simeq SNR_3$ and therefore

$$SNR_{3net} = \sqrt{3} \cdot SNR. \quad (14)$$

Being all three detectors co-located, a noise glitch can degrade $SNR_{1,2,3}$ by a value $0 < X < 1$, i.e., we make the simplistic assumption that the noise glitch propagates equally in each detector. Hence, we can write

$$\begin{aligned} SNR_{3net}^{new} &= \sqrt{(X \cdot SNR_1)^2 + (X \cdot SNR_2)^2 + (X \cdot SNR_3)^2} = \\ &= X \cdot \sqrt{3} \cdot SNR. \end{aligned} \quad (15)$$

This way, the reduction factor X is the same for both the network and the single detector SNR.

On the other hand, if we imagine the ideal situation in which we have a 2L network with each detector oriented so that both detectors observe an event with the same SNR, a noise glitch will affect only the SNR of one detector with respect to the other by a factor $0 < X_s < 1$. Hence, we can write:

$$SNR_{2net} = \sqrt{SNR_1^2 + SNR_2^2} = \sqrt{(X_s \cdot SNR_2)^2 + SNR_2^2}, \quad (16)$$

which gives

$$SNR_{2net} = \sqrt{X_s^2 + 1} \cdot SNR_2. \quad (17)$$

From the results shown in Table II, we see that, in the 50th percentile case and considering Sardinia as the ideal case, because it shows better performance with respect to EMR, we get an average $X_{SAR}^{EMR} = 0.83$. This means that an ET triangle at the EMR site observes events with $SNR_{net}^{EMR} = 0.83 \cdot SNR_{net}^{SAR}$.

We can now answer the question what would have to be X_s to have a 0.83 reduction in the network SNR in the 2L case. Let us suppose that both detectors observe an event with the same $SNR = 14$, hence $SNR_{2net} = 19.8$. Using Equation 17

$$0.83 \cdot SNR_{2net} = \sqrt{X_s^2 + 1} \cdot SNR, \quad (18)$$

Case	SNR/SNR _{DESIGN}		EVENTS WITH SNR < 12		SNR _{EMR} /SNR _{SAR}
	Sardinia	EMR	Sardinia	EMR	
10th percentile	+6%	+2.5%	-2%	-1%	0.96
50th percentile	+5%	-12%	-1.5%	6%	0.83
90th percentile	-2.5%	-37%	3%	24%	0.69

TABLE III: Summary of the SNR performance for the Sardinia and EMR candidate sites in the case of BNS mergers. The negative figures under the events with SNR < 12 highlight an improvement in the fraction of recovered events with respect to the design case.

we infer that

$$X_s = \sqrt{0.83 \frac{SNR_{2net}}{SNR} - 1} = 0.49. \quad (19)$$

This means that, to experience a reduction in the 2L network SNR comparable to what we observe in the comparison between Sardinia and EMR in the triangle configuration, one of the two detectors in the network can have the SNR reduced up to 50%. Moreover, if we recall the assumption (Equation 15) for which, in the triangle configuration, X is the same for both the network and the single detectors and that the comparison between EMR and Sardinia never shows, on average, X less than 0.69 in the worst possible scenario, we conclude that, for a single detector $SNR = 14$, the 2L network would have the network SNR reduced only by a factor 0.87 in this case.

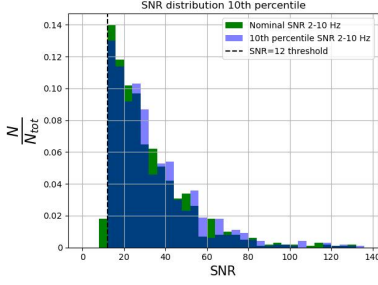
VIII. CONCLUSIONS AND FUTURE PLANS

We investigated the impact of site dependent ambient noise on the low-frequency sensitivity of ET at the two sites candidate to host ET: the Sos Enattos site in Sardinia, Italy, and the Terziet side in the EMR region at the border between The Netherlands and Belgium. According to the currently available site characterization data, we focused on the impact of the seismic noise contribution to NN which is more prominent between 2 Hz and 10 Hz. Using the 10th, 50th and 90th percentile of the seismic spectra distributions covering two years at the two candidate sites, we inferred the impact on the ET sensitivity curve. We found that the Sardinia candidate site has the lowest impact on the ET sensitivity if compared to the effect of local ambient noise recorded at EMR, which, on the other hand, appears to have a larger impact. These results were obtained without considering any NN suppression factor in Equation 5. As a consequence, we expect that these results may provide some relevant information about the design of NN suppression systems for ET that will be different for each candidate site. In fact, Sardinia appears to be compliant with the requirements of ET already without considering any NN suppression factor, whereas the larger impact on the design sensitivity of the EMR site will require dedicated seismometer arrays for noise subtraction [89] to reduce its impact on the design sensitivity. These results suggests

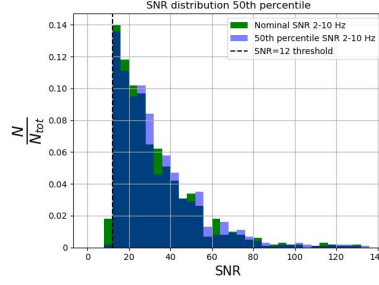
that Sardinia is also an ideal location for research and development activities in low noise environments. For what concerns achievable NN suppression factors, previous works [65, 90, 91] showed that by optimizing NN cancellation for a specific frequency may lead up to a factor 10 suppression. Nevertheless, at other frequencies the factor would be $\simeq 2$ [90]. Broadband NN cancellation, on the other hand, would not achieved a suppression factor better than 3 [90]. It should also be pointed out that the signals considered in this work span a wide range of frequencies, therefore we should focus on broadband NN cancellation. Finally, NN cancellation comes at the cost of a huge computational and financial effort. For example, considering the achievement of a factor 3 NN suppression factor as the most reasonable assumption for ET, it would require a few tens of seismometers in boreholes per test mass [90]. Since the ET triangle will have 12 test masses, we should expect $\mathcal{O}(100)$ sensors placed in boreholes around the test masses. The main challenges would be determining where to drill the boreholes to achieve effective NN reduction and the processing of 3D data for the NN cancellation algorithms (being on surface, current detectors only require 2D data).

The different impact of the Sardinia and EMR sites on the ET sensitivity translates into an influence on the signal SNR at low frequency for those astrophysical sources for which low-frequency sensitivity plays an important role, i.e. IMBH and BNS mergers. Using the source parameters present in astrophysical catalogs obtained from population studies, we generated a set of waveforms and injected them into ET noise simulated according to the sensitivity curves derived from local ambient noise. SNR has then been calculated using the matched filter SNR. Comparing the resulting SNR distributions against the benchmark case obtained from the ET design sensitivity curve, we find that local ambient noise has a lower impact on the signal SNR in Sardinia, which is very close to design. The EMR site shows a higher SNR degradation, with respect to design (Figures from 10 to 13).

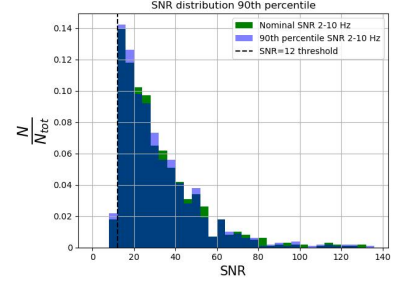
Given the ET early warning requirements for BNS and the time to merger at 10 Hz of these signals, a significant degradation of the signal SNR may affect the ET early warning capabilities and hinder the possibility of extensive multimessenger observation campaigns for a number of events larger than expected. In this sense, we have also inferred the cumulative distributions of the time to merger at detection and found that this is most likely to happen at EMR than Sardinia (Figures 14 and 15).



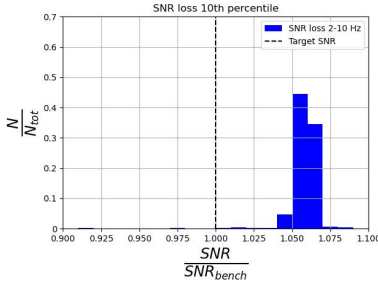
(a) Sardinia Nominal SNR distribution (green) and SNR distribution using the 10th percentile ET sensitivity (blue).



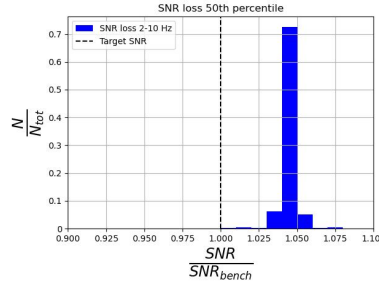
(b) Sardinia nominal SNR distribution (green) and SNR distribution using the 50th percentile ET sensitivity (blue).



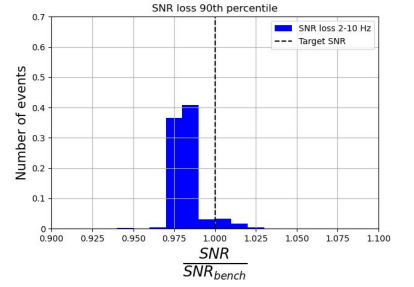
(c) Sardinia nominal SNR distribution (green) and SNR distribution using the 90th percentile ET sensitivity (blue).



(d) Sardinia SNR/ SNR_{design} using the 10th percentile ET sensitivity.



(e) Sardinia SNR/ SNR_{design} using the 50th percentile ET sensitivity.



(f) Sardinia SNR/ SNR_{design} using the 90th percentile ET sensitivity.

FIG. 10: IMBH SNR distributions for the Sardinia candidate site. In the top row, the SNR = 12 threshold is marked with a black dashed line. In the bottom row, the black dashed line represents the equality between the SNR measured in the design case with the cases of the modified ET curves. The non overlapped green SNR bin under the SNR threshold highlights the fact that there are some events lost in the design case but recovered in the best possible recorded noise conditions.

These issues could be solved only with the use of appropriate NN suppression that should be more prominent at the EMR site.

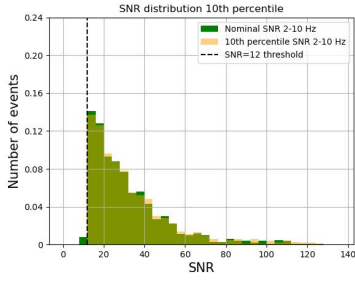
In future, we will follow up this study to consider the ET 2L configuration and assess the impact of site dependent noise on a detector network composed of two widely separated detectors that are not affected by the same noise sources at the same times. Perhaps, in this case, the presence of the most sensitive interferometer in Sardinia could make the impact of the worse EMR sensitivity on the detection rates less dramatic. We also plan to quantify the effect of local ambient noise on the source sky localization areas issued by early warnings using currently available detection pipelines. This will further ex-

pand the overview of the impact of ambient noise on the detectability of GW sources.

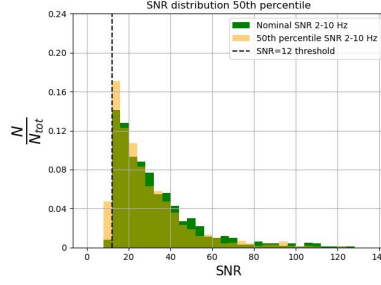
ACKNOWLEDGMENTS

The authors gratefully acknowledge dr. M. Mancarella, prof. T. Bulik, dr. S. Koley and dr. J. van Heijningen for their helpful comments and advices that significantly improved the presentation of this work. Dr. M. Di Giovanni would also like to acknowledge dr. E. Codazzo for providing the necessary information to correctly download and interpret the information contained in the astrophysical catalogs.

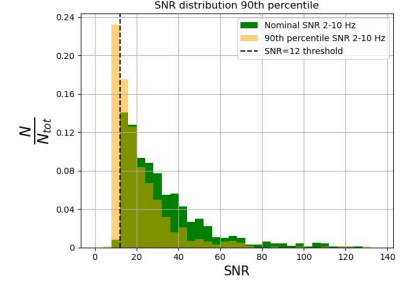
-
- [1] LVC Collaboration, GWTC-1: A gravitational-wave transient catalog of compact binary mergers observed by LIGO and Virgo during the first and second observing runs, *Phys. Rev. X* **9**, 031040 (2019).
 - [2] LVK Collaboration, GWTC-2: Compact binary coalescences observed by LIGO and Virgo during the first half of the third observing run, *Phys. Rev. X* **11**, 021053 (2021).
 - [3] LVK Collaboration, GWTC-3: Compact binary coalescences observed by LIGO and Virgo during the second part of the third observing run, *Phys. Rev. X* **13**, 041039 (2023).
 - [4] Virgo Collaboration, Advanced Virgo: a second-generation interferometric gravitational wave detector, *Classical Quant. Grav.* **32**, 024001 (2014).
 - [5] LSC Collaboration, Advanced ligo, *Classical Quant. Grav.* **32**, 074001 (2015).
 - [6] KAGRA Collaboration, Kagra: 2.5 generation interferometric gravitational wave detector, *Nat. Astron.* **3**, 35 (2019).
 - [7] Maggiore *et al.*, Science case for the einstein telescope, *JCAP* **2020** (03), 050.
 - [8] Branchesi *et al.*, Science with the Einstein Telescope: a comparison of different designs, *JCAP* **2023** (07), 068.
 - [9] Reitze *et al.*, Cosmic Explorer: The US contribution to gravitational-wave astronomy beyond LIGO, arxiv.org/abs/1907.04833 (2019).
 - [10] Evans *et al.*, A horizon study for Cosmic Explorer: Science, observatories, and community, arxiv.org/abs/2109.09882 (2021).
 - [11] Hall *et al.*, Cosmic Explorer: A next-generation ground-based gravitational-wave observatory, *Galaxies* **10**, 10.3390/galaxies10040090 (2022).
 - [12] Punturo *et al.*, The Einstein Telescope: a third-generation gravitational wave observatory, *Classical Quant. Grav.* **27**, 194002 (2010).
 - [13] ET Science Team, The Einstein Telescope: a third-generation gravitational wave observatory, *Classical Quant. Grav.* **27**, 194002 (2010).
 - [14] ET Science Team, Einstein gravitational wave telescope conceptual design study, ET-0106C-10 (2011).
 - [15] ET Science Team, Design report update for the Einstein Telescope, ET-0028A-20 (2020).
 - [16] Iacovelli *et al.*, Combining underground and on-surface third-generation gravitational-wave interferometers, *Journal of Cosmology and Astroparticle Physics* **2024** (10), 085.
 - [17] Hutt *et al.*, Broadband seismic noise attenuation versus depth at the albuquerque seismological laboratory, *Bulletin of the Seismological Society of America* **107**, 1402 (2017), <https://pubs.geoscienceworld.org/ssa/bssa/article-pdf/107/3/1402/2641899/BSSA-2016187.1.pdf>.
 - [18] Branchesi, Multi-messenger astronomy: gravitational waves, neutrinos, photons, and cosmic rays, *Journal of Physics: Conference Series* **718**, 022004 (2016).
 - [19] A. H. Nitz and T. D. Canton, Pre-merger localization of compact-binary mergers with third-generation observatories, *The Astrophysical Journal Letters* **917**, L27 (2021).
 - [20] Q. Hu and J. Veitch, Rapid premerger localization of binary neutron stars in third-generation gravitational-wave detectors, *The Astrophysical Journal Letters* **958**, L43 (2023).
 - [21] LVC Collaboration, Multi-messenger observations of a binary neutron star merger, *Astrophys. J.* **848**, L12 (2017).
 - [22] Branchesi, Gw170817: The dawn of multi-messenger astronomy including gravitational waves, in *Multiple Messengers and Challenges in Astroparticle Physics*, edited by R. Aloisio, E. Coccia, and F. Vissani (Springer International Publishing, Cham, 2018) pp. 489–497.
 - [23] Radice *et al.*, GW170817: Joint constraint on the neutron star equation of state from multimessenger observations, *Astroph. Jour. Lett.* **852**, L29.
 - [24] LVC Collaboration, A gravitational-wave standard siren measurement of the Hubble constant, *Nature* **551**, 85 (2017).
 - [25] Koliopanos, Intermediate Mass Black Holes: A Review, *PoS MULTIF2017*, 051 (2018).
 - [26] Mezcua, Observational evidence for intermediate-mass black holes, *International Journal of Modern Physics D* **26**, 1730021 (2017), <https://doi.org/10.1142/S021827181730021X>.
 - [27] Greene *et al.*, A gravitational-wave standard siren measurement of the Hubble constant, *Ann. Rev. of Aston. Astroph.* **58**, 257 (2020).
 - [28] Longuet-Higgins, A theory of the origin of microseisms, *Phil. Trans. R. Soc. Lond.* **243**, 35 (1950).



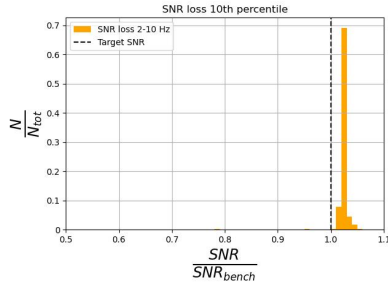
(a) EMR Nominal SNR distribution (green) and SNR distribution using the 10th percentile ET sensitivity (blue).



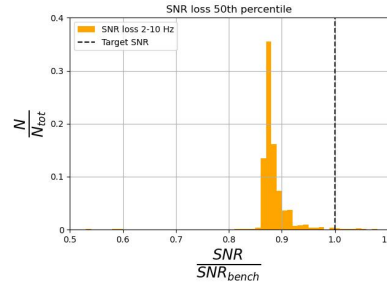
(b) EMR Nominal SNR distribution (green) and SNR distribution using the 50th percentile ET sensitivity (blue).



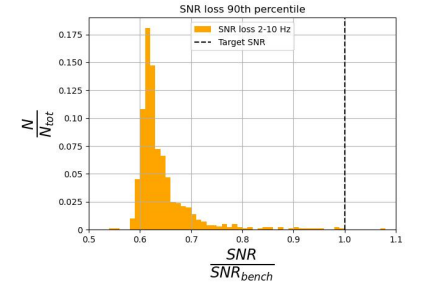
(c) EMR Nominal SNR distribution (green) and SNR distribution using the 90th percentile ET sensitivity (blue).



(d) SNR/SNR_{design} at EMR using the 10th percentile ET sensitivity.



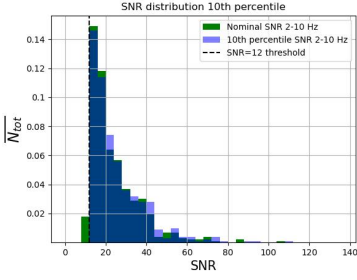
(e) SNR/SNR_{design} at EMR using the 50th percentile ET sensitivity.



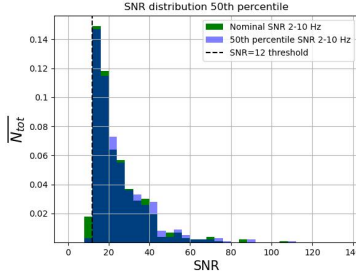
(f) SNR/SNR_{design} at EMR using the 90th percentile ET sensitivity.

FIG. 11: IMBH SNR distributions for the EMR candidate site. In the top row, the $SNR = 12$ threshold is marked with a black dashed line. In the bottom row, the black dashed line represents the equality between the SNR measured in the design case with the cases of the modified ET curves. The non overlapped green SNR bin under the SNR threshold highlights the fact that there are some events lost in the design case but recovered in the best possible recorded noise conditions.

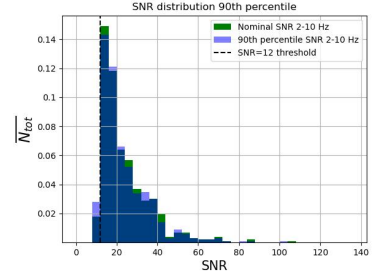
- [29] Ward and Crawford, Wind-induced vibrations and building modes, *Bull. Seism. Soc. Am.* **56**, 793 (1966).
- [30] Cessaro, Sources of primary and secondary microseisms, *Bull. Seism. Soc. Am.* **84**, 142 (1994).
- [31] Withers *et al.*, High-frequency analysis of seismic background noise as a function of wind speed and shallow depth, *B. Seismol. Soc. Am.* **86**, 1507 (1996).
- [32] Acernese *et al.*, Properties of seismic noise at the Virgo site, *Classical and Quantum Gravity* **21**, S433 (2004).
- [33] Coward *et al.*, Characterizing seismic noise in the 2–20 hz band at a gravitational wave observatory, *Review of scientific instruments* **76**, 044501 (2005).
- [34] Virgo Collaboration, Environmental noise studies at Virgo, *J. Phys. Conf. Ser.* **32**, 80 (2006).
- [35] Burtin *et al.*, Spectral analysis of seismic noise induced by rivers: A new tool to monitor spatiotemporal changes in stream hydrodynamics, *J. Geophys. Res.-Sol. Ea.* **113** (2008).
- [36] Anthony *et al.*, The widespread influence of great lakes microseisms across the midwestern united states revealed by the 2014 polar vortex, *Geop. Res. Lett.* **45**, 3436 (2018).
- [37] Smith and Tape, Seismic noise in central alaska and influences from rivers, wind, and sedimentary basins, *JGR Solid Earth* **124**, 11678 (2019).
- [38] Dybing *et al.*, Two mechanisms explain microseisms with periods 3 to 300 s, *Geophys. Res. Lett.* **42**, 765 (2019).
- [39] Virgo Collaboration, The Virgo O3 run and the impact of the environment, *Classical and Quantum Gravity* **39**, 235009 (2022).
- [40] Anthony *et al.*, Seismic background noise levels across the continental united states from usarray transportable array: The influence of geology and geography, *Bulletin of the Seismological Society of America* **112**, 646 (2022), <https://pubs.geoscienceworld.org/ssa/bssa/article-pdf/112/2/646/5638811/bssa-2021176.1.pdf>.
- [41] Saccorotti *et al.*, Seismic noise by wind farms: a case study from the Virgo gravitational wave observatory, italy, *Bull. Seis. Soc. Am.* **101** (2011).
- [42] Piccinini *et al.*, COVID-19 lockdown and its latency in Northern Italy: Seismic evidence and socio-economic interpretation, *Sci. Rep.* **10**, 16487 (2020).
- [43] Poli *et al.*, The 2020 coronavirus lockdown and seismic monitoring of anthropic activities in Northern Italy, *Sci. Rep.* **10**, 9404 (2020).
- [44] Virgo Collaboration, Properties of seismic noise at the Virgo site, *Classical Quan. Grav.* **21**, S433 (2004).
- [45] Virgo Collaboration, The seismic superattenuators of the Virgo gravitational-wave interferometer, *J. Low Freq. noise V. A.* **30**, 63 (2011).
- [46] Virgo Collaboration, Characterization of the Virgo seismic environment, arXiv:1108.1598 (2011).
- [47] Koley, *Sensor networks to measure environmental noise at gravitational wave detector sites*, Ph.D. thesis, Vrije Universiteit Amsterdam (2020).
- [48] Fiori *et al.*, Environmental noise in gravitational-wave interferometers, in *Handbook of Gravitational Wave Astronomy* (Springer Singapore, Singapore, 2020) pp. 1–72.
- [49] Accadia *et al.*, Noise from scattered light in Virgo’s second science run data, *Classical and Quantum Gravity* **27**, 194011 (2010).
- [50] Martynov *et al.*, Sensitivity of the Advanced LIGO detectors at the beginning of gravitational wave astronomy, *Phys. Rev. D* **93**, 112004 (2016).
- [51] Saulson, Terrestrial gravitational noise on a gravitational wave antenna, *Phys. Rev. D* **30**, 732 (1984).
- [52] Beccaria *et al.*, Relevance of newtonian seismic noise for the Virgo interferometer sensitivity, *Classical Quant. Grav.* **15**, 3339 (1998).
- [53] Harms, Terrestrial gravity fluctuations, *Liv. Rev. Rel.* **22**, 10.1007/s41114-019-0022-2 (2019).
- [54] Amann *et al.*, Site-selection criteria for the Einstein Telescope, *Rev. Sci. Instr.* **91**, 094504 (2020).
- [55] Naticchioni *et al.*, Microseismic studies of an underground site for a new interferometric gravitational wave detector, *Classical Quant. Grav.* **31** (2014).
- [56] Naticchioni *et al.*, Characterization of the Sos Enattos site for the Einstein Telescope, *J. Phys.: Conf. Ser.* **1468** (2020).
- [57] Di Giovanni *et al.*, A seismological study of the Sos Enattos area—the Sardinia candidate site for the Einstein Telescope, *Seismol. Res. Lett.* **92**, 352 (2021).
- [58] Di Giovanni *et al.*, Temporal variations of the ambient seismic field at the Sardinia candidate site of the Einstein Telescope, *Geophysical Journal International* **234**, 1943 (2023), <https://academic.oup.com/gji/article-pdf/234/3/1943/50285042/ggad178.pdf>.
- [59] Allocca *et al.*, Seismic glitchness at Sos Enattos site: impact on intermediate black hole binaries detection efficiency, *Eur. Phys. J. Plus* , 511 (2021).
- [60] Saccorotti *et al.*, Array analysis of seismic noise at the Sos Enattos mine, the italian candidate site for the einstein telescope, *Eur. Phys. J. Plus* **138**, 793 (2023).
- [61] Koley *et al.*, Characteristics of surface wave green’s function for anisotropic ambient seismic noise field — a case study in limburg, the netherlands, *First Break* **37**, 83 (2019).
- [62] Bader *et al.*, Newtonian-noise characterization at terziet in limburg—the euregio meuse–rhine candidate site for einstein telescope, *Classical and Quantum Gravity* **39**, 025009 (2022).
- [63] Koley *et al.*, Surface and underground seismic characterization at terziet in limburg—the euregio meuse–rhine candidate site for einstein telescope, *Classical and Quantum Gravity* **39**, 025008 (2022).
- [64] Janssens *et al.*, Correlated 0.01Hz–40Hz seismic and Newtonian noise and its impact on future gravitational-wave detectors, *PRD* **137**, 102002 (2024).
- [65] Badaracco *et al.*, Optimization of seismometer arrays for the cancellation of Newtonian noise from seismic body waves, *Class. Quantum Grav.* **36**, 10.1088/1361-6382/ab28c1 (2019).
- [66] W. Commons, Sardinia relief location map (2010), https://commons.wikimedia.org/wiki/File:Italy_Sardinia_relief_location_map.svg.
- [67] W. Commons, Netherlands relief location map (2013), https://commons.wikimedia.org/wiki/File:Netherlands_relief_location_map.svg.
- [68] W. Commons, Europe relief location map (2010), https://commons.wikimedia.org/wiki/File:Europe_relief_laea_location_map.jpg.
- [69] LVK collaboration, Search for intermediate-mass black hole binaries in the third observing run of Advanced LIGO and Advanced Virgo, *A&A* **659**, A84 (2022).
- [70] LVC Collaboration (LIGO Scientific Collaboration and Virgo Collaboration), Gw190521: A binary black hole merger with a total mass of $150 M_{\odot}$, *Phys. Rev. Lett.* **125**, 101102 (2020).



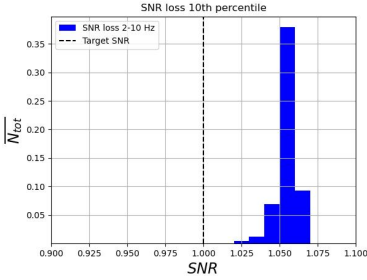
(a) Sardinia Nominal SNR distribution (green) and SNR distribution using the 10th percentile ET sensitivity (blue).



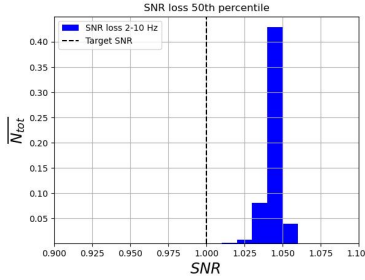
(b) Sardinia nominal SNR distribution (green) and SNR distribution using the 50th percentile ET sensitivity (blue).



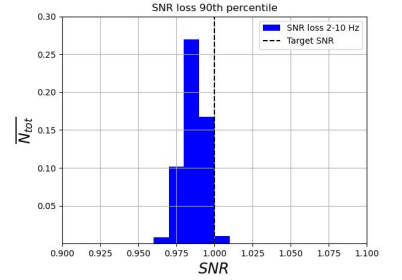
(c) Sardinia nominal SNR distribution (green) and SNR distribution using the 90th percentile ET sensitivity (blue).



(d) Sardinia SNR/ SNR_{design} using the 10th percentile ET sensitivity.



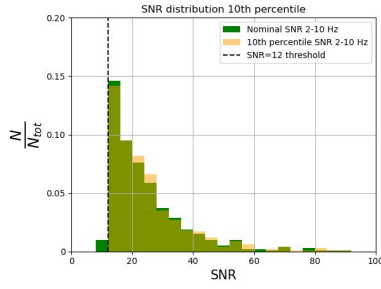
(e) Sardinia SNR/ SNR_{design} using the 50th percentile ET sensitivity.



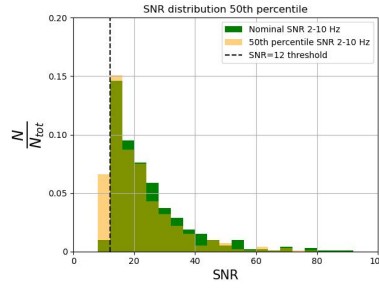
(f) Sardinia SNR/ SNR_{design} using the 90th percentile ET sensitivity.

FIG. 12: BNS SNR distributions for the Sardinia candidate site. In the top row, the $SNR = 12$ threshold is marked with a black dashed line. In the bottom row, the black dashed line represents the equality between the SNR measured in the design case with the cases of the modified ET curves. The non overlapped green SNR bin under the SNR threshold highlights the fact that there are some events lost in the design case but recovered in the best possible recorded noise conditions.

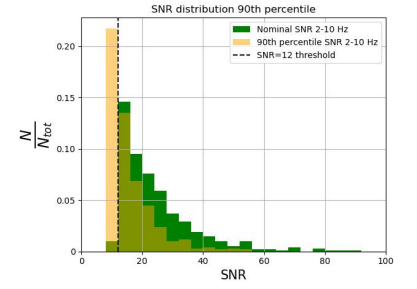
- [71] LVK Collaboration, Search for intermediate-mass black hole binaries in the third observing run of Advanced LIGO and Advanced Virgo, *A & A* **659**, A84 (2022).
- [72] GRAVITY Collaboration *et al.*, Where intermediate-mass black holes could hide in the galactic centre - a full parameter study with the s2 orbit, *A&A* **672**, A63 (2023).
- [73] Maggiore, *Gravitational Waves - Volume 1* (Oxford University Press, New York, 2008).
- [74] Husa *et al.*, Frequency-domain gravitational waves from nonprecessing black-hole binaries. i. new numerical waveforms and anatomy of the signal, *Phys. Rev. D* **93**, 044006 (2016).
- [75] Khan *et al.*, Frequency-domain gravitational waves from nonprecessing black-hole binaries. ii. a phenomenological model for the Advanced detector era, *Phys. Rev. D* **93**, 044007 (2016).
- [76] Dietrich *et al.*, Improving the nrtdal model for binary neutron star systems, *Phys. Rev. D* **100**, 044003 (2019).
- [77] Miller *et al.*, Enabling multimessenger astronomy with continuous gravitational waves: Early warning and sky localization of binary neutron stars in the einstein telescope, *Phys. Rev. D* **109**, 043021 (2024).
- [78] Beker *et al.*, Seismic attenuation technology for the Advanced Virgo gravitational wave detector, *Pyhs. Proc.* **37**, 1389 (2012).
- [79] Beker *et al.*, Subterranean ground motion studies for the Einstein Telescope, *Classical Quant. Grav.* **32**, 025002 (2015).
- [80] Harms *et al.*, A lower limit for Newtonian-noise models of the Einstein Telescope, *The European Physical Journal Plus* **137**, 687 (2022).
- [81] Nitz *et al.*, gwastro/pycbc: v2.3.3 release of pycbc (2024).
- [82] LVK Collaboration, LVK Algorithm Library - LALSuite, Free software (GPL) (2018).
- [83] Allen *et al.*, FINDCHIRP: An algorithm for detection of gravitational waves from inspiraling compact binaries, *Phys. Rev. D* **85**, 122006 (2012).
- [84] Usman *et al.*, The pycbc search for gravitational waves from compact binary coalescence, *Classical and Quantum Gravity* **33**, 215004 (2016).
- [85] Peterson, *Observations and modeling of seismic background noise*, Tech. Rep. (US Geological Survey, 1993).
- [86] Iacovelli *et al.*, BBH and BNS source catalogs used for the CoBA science study (2023), <https://apps.et-gw.eu/tds/?r=18321>.
- [87] Mapelli *et al.*, The cosmic evolution of binary black holes in young, globular, and nuclear star clusters: rates, masses, spins, and mixing fractions, *Monthly Notices of the Royal Astronomical Society* **511**, 5797 (2022), <https://academic.oup.com/mnras/article-pdf/511/4/5797/42778203/stac422.pdf>.
- [88] Santoliquido *et al.*, The cosmic merger rate density of compact objects: impact of star formation, metallicity, initial mass function, and binary evolution, *Monthly Notices of the Royal Astronomical Society* **502**, 4877 (2021), <https://academic.oup.com/mnras/article-pdf/502/4/4877/36409570/stab280.pdf>.
- [89] van Beveren *et al.*, A study of deep neural networks for Newtonian noise subtraction at Terziet in Limburg—the Euregio Meuse-Rhine candidate site for Einstein Telescope, *Classical Quant. Grav.* **40**, 205008 (2023).
- [90] Badaracco *et al.*, Machine learning for gravitational-wave detection: surrogate Wiener filtering for the prediction and optimized cancellation of newtonian noise at Virgo, *Classical and Quantum Gravity* **37**, 195016 (2020).
- [91] Koley *et al.*, Adaptive algorithms for low-latency cancellation of seismic newtonian-noise at the Virgo gravitational-wave detector, *Phys. Rev. D* **110**, 022002 (2024).



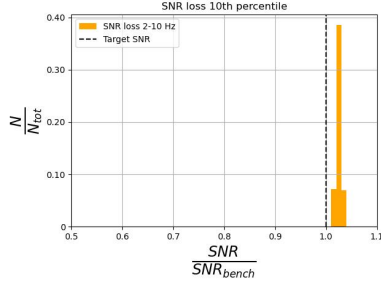
(a) EMR Nominal SNR distribution (green) and SNR distribution using the 10th percentile ET sensitivity (blue).



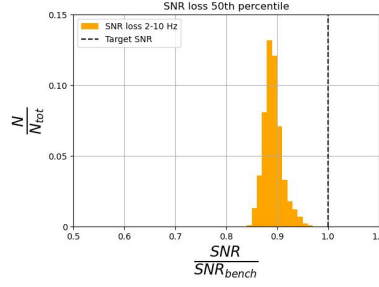
(b) EMR Nominal SNR distribution (green) and SNR distribution using the 50th percentile ET sensitivity (blue).



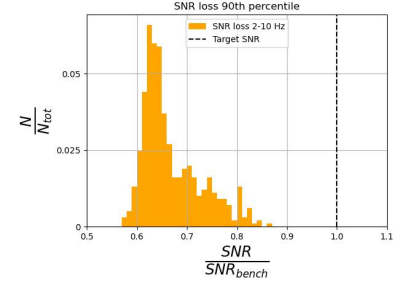
(c) EMR Nominal SNR distribution (green) and SNR distribution using the 90th percentile ET sensitivity (blue).



(d) $\text{SNR}/\text{SNR}_{\text{design}}$ at EMR using the 10th percentile ET sensitivity.

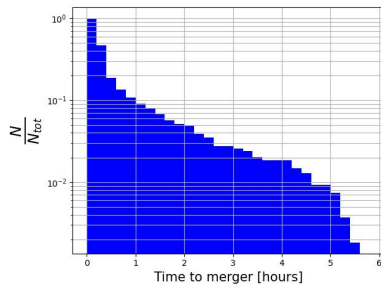


(e) $\text{SNR}/\text{SNR}_{\text{design}}$ at EMR using the 50th percentile ET sensitivity.

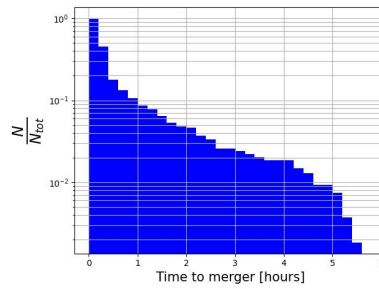


(f) $\text{SNR}/\text{SNR}_{\text{design}}$ at EMR using the 90th percentile ET sensitivity.

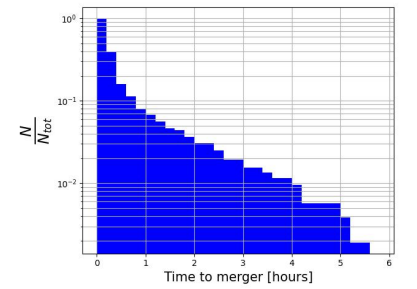
FIG. 13: BNS SNR distributions for the EMR candidate site. In the top row, the $\text{SNR} = 12$ threshold is marked with a black dashed line. In the bottom row, the black dashed line represents the equality between the SNR measured in the design case with the cases of the modified ET curves. The non overlapped green SNR bin under the SNR threshold highlights the fact that there are some events lost in the design case but recovered in the best possible recorded noise conditions.



(a)



(b)



(c)

FIG. 14: Cumulative distributions of the time to merger at detection for the Sardinia site.

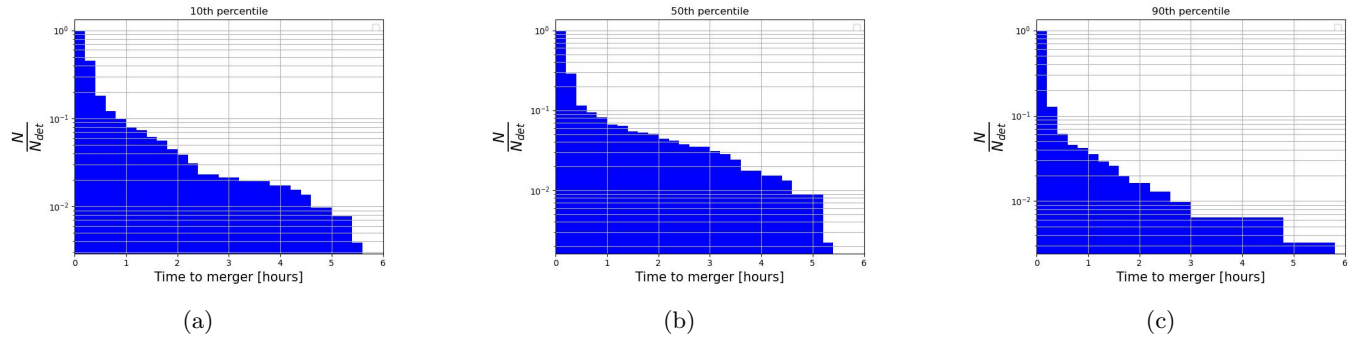


FIG. 15: Cumulative distributions of the time to merger at detection for the EMR site.